

RADAR SENSING OF THIN SURFACE LAYERS AND NEAR-SURFACE BURIED OBJECTS

Kevin O'Neill₁
Cold Regions Research and Engineering Laboratory
Hanover, NH 03755

ABSTRACT

A robust ground penetrating radar (GPR) signal processing approach is developed and applied to the sensing of surface soil and ice/water layers as well as near-surface buried objects. The principal technique relies on a reference set of waveforms which are tested for optimal matching with measured radar reflections to be analyzed. In principle the reference set can be based on measurements as well as on model output, with the latter employed here. Even when layers are quite thin relative to the incident wavelength or pulse, the approach provides accurate information on layer characteristics, particularly thickness. The method assumes a well defined transmit signal and hence is best used with antennas elevated above the surface. In tests using UHF pulses on lab and field ice and on thawing soil, the system offers approximately an order of magnitude improvement in layer resolution relative to more traditional methods. Also, in the process of its signal matching calculations the procedures provide a numerical indication of the reliability of each result. In application to thawing soil, simulations suggest that one can address a wide variety of conditions using quite a limited set of reference signals. By detecting the thin-layer effect from soil over a buried metallic object, the system also locates near-surface targets when their reflections cannot be separated in time from ground surface returns. An alternative system also succeeds in detecting near-surface objects under the same conditions by detecting wavelet

dispersion. This is done without reliance on specific details of transmit wavelet or reflected signals. Using this approach, we show that a mine-like target is detectable in a wet clayey soil when the ground is frozen but not when it is thawed.

INTRODUCTION

In GPR field surveying, one usually obtains the best antenna-ground coupling when the antenna is in contact with the ground. However, this imposes considerable limitations on GPR use. Airborne surveying can cover much greater areas quickly and enables one to profile inhospitable terrain. Whether airborne or not, elevated antennas and sensing apparatus also avoid damage to sensitive environments and can evaluate terrain trafficability without intrusion. Elevated systems are also particularly appropriate when one is specifically interested in the ground or water surface layer itself.

For most subsurface sensing purposes, one must accept some tradeoff between resolution and penetration. Signal attenuation in water bearing media becomes severe as one proceeds upwards towards or higher than 1 GHz in frequency. In cold water with dc conductivity representative of typical freshwater bodies, inherent lossiness engenders signal loss of more than 90 dB/m (see below). Scattering losses also mount with frequency. Lower frequencies achieve much greater penetration but may be inadequate to resolve layers of practical interest. In estimating the bearing capac-

ity of ice, for example, one may need to distinguish layers as thin as a few centimeters [1]. A typical high frequency, short pulse GPR wavelet with center frequency around 900 MHz has a duration approaching 4 ns. While this might be regarded as a high resolution wavelet for many geophysical purposes, its length in ice of more than 60 cm limits its usefulness for thin ice evaluation. Similarly, in making trafficability determinations for thawing soil one needs to identify conditions within and beyond the critical thaw depths of five to ten cm or so [2-4]. Choosing a lower frequency short pulse system to enhance penetration in the moist soil, we consider a 600 MHz center frequency and typical wavelet duration of 5 to 6 ns. Even when the dielectric constant of moist soil is as high as 16, the subsurface wavelet length still approaches 45 cm. Thus, for these and other similar applications we require innovative methods that allow us to sense relatively thin layers while remaining with low enough frequencies to accomplish penetration.

While for some time there has been a vast body of work on geophysical signal processing for detecting interfaces (eg [5], [6]), there is little available for discriminating interfaces very close together. It has been recognized that interferometric techniques may offer some advantages in terms of resolution. Rossiter et al. [7] employ a technique with transmit and receiving antennas at a succession of separations. By detecting the interference pattern between direct transmission and that in various modes through an ice layer, they are able to characterize a layer greater than about 0.2 free space wavelengths in thickness. This sort of approach has the disadvantage that it is measurement intensive (two antennas, many separations) and operates in contact with the surveyed surface. As elaborated below, one might infer surface layer characteristics such as thickness from elevated normal incidence surveying, by examining the cyclical pattern in the layer system frequency response (e.g. [8]). However, this assumes that one has a sufficient bandwidth to discern the required patterns or to locate critical points in them. Often this is not easily accomplished, due either to radar system limitations or to the failure of high frequen-

cies to penetrate the ground. Special measures must then be employed to infer a larger pattern from measurement of a limited portion of it (e.g. [9]). By performing enough measurements of different sorts, one might be able to infer surface layer characteristics by resorting to the many processing avenues in the growing body of inverse techniques. However, here we seek simple approaches that minimize both measurement and subsequent analysis and computation.

The two approaches pursued here are a *waveform recognition* approach and a *wavelet dispersion* or *energy duration* approach. In the latter we detect subsurface, near-surface reflections by observing the spreading out of the input wavelet in time. In the waveform recognition approach, to which most attention is devoted in what follows, we operate in the time domain and seek to identify characteristic interference patterns between echoes from interfaces that are near one another. This is somewhat akin to a matched filter approach to the data, with utilization of reference signal forms from model calculations or previous measurements. We infer the characteristics of a surveyed surface layer by determining which waveforms, corresponding to known layer systems, best match measured data. The section immediately below outlines the basic features of reflections from closely spaced interfaces, proceeding then to the waveform recognition strategy. This is followed by exposition of the underlying theory for modeling layered system behavior, linked to computational considerations. In the Results section that follows, the approach is applied to thin ice sheets under controlled or closely observed conditions, to wet and dry field ice on a river, and to thaw layers on frozen soil. Despite the lossiness of cold water, we argue that features within or below wet ice can actually become more visible under certain conditions when the water layer on top of the ice becomes thicker. Simulations suggest generalizations of the layer analysis to include surface soil situations featuring continuous variation of moisture content and hence of dielectric content with depth. Lastly we show successful detection of mine-like targets near the surface of moist soil and in frozen clay.

BACKGROUND AND METHOD

Behavior of the Physical System and Analytical Approach

Our approaches rest on a simple physical model of a layered system, as illustrated in Figure 1. The upper half space (medium 0) consists of air; the subject layer is medium 1, underlain by a half space containing medium 2. We assume that each medium is homogeneous and that the surveying radar beam is a normally incident plane wave. The beam reflects back from the upper (media 0:1) and lower (media 1:2) interfaces, in a primary surface return (R_0) followed by a sequence of multiple reflections (R_1, R_2, \dots). The two reflection time sequences in the figure illustrate markedly different relations between the magnitude and sign in the sequence of returns, depending upon whether the layer is more or less electrically dense than the substrate (medium 2). In the case with an ice layer over water, the largest return is R_1 , from the ice/water interface; R_0 and R_1 are both negative, and R_0 is likely to be significant relative to R_1 . In the case with water over ice, the largest reflection is the surface return, R_0 ; R_1 is opposed in sign and is much smaller. For illustrative purposes, the pulse magnitudes in the figure were determined for lossless media. In fact, depending upon the depth of the surface water layer, its lossiness could well make all other returns insignificant with respect to R_0 . Below we cite loss rates for cold water of more than 90 dB/m at a frequency of 1 GHz. Thus, in making a round trip across a 3.5 cm deep layer of water, a 1 GHz signal would suffer more than a factor of four diminution in power, beyond what is implied by the lossless relations shown in the figure.

Figure 2 shows some comparable time sequences arising from real wavelets, as opposed to the idealized pulses in Figure 1. These were produced from a GSSI 101C antenna system (details in [10]) and the computational framework presented below. Reflections from a bare foil sheet supplied the wavelet $s(t)$, shown in curve (a). Curve (b) shows the calculated reflection from an ice layer about 7 cm thick on top of the foil, based

on the model; curve (c) is a measured reflection for that thickness. (The curves in the figure have been shifted in time differently to facilitate comparison). Similarity between the synthetic echo and the recorded one are clear; one sees some leading content corresponding to R_0 emerging from the front of the dominant R_1 response. The similarity between the recorded and the synthetic echoes (d) and (e) for about 17 cm ice thickness is even more readily apparent. Here the R_0 and R_2 components emerge farther from the leading and trailing edges of the larger R_1 response. In the synthetic echo (f) for a 24 cm thick ice layer, R_0 and R_2 components have completely separated from R_1 . In traditional approaches we might estimate the thickness of the ice layer by timing the delay between these distinct R_i components. While impressive geophysical techniques abound, basically the common wisdom summed up by Davis and Annan [11] still applies on the question of resolution here. Available deconvolution techniques will typically fail to indicate this delay when there is much overlap between the various echo components.

One approach to distinguishing different echoes of the sort shown is to note different degrees of dispersion corresponding to different layer thicknesses. That is, beyond any frequency dependent losses incurred by the wavelet as it bounces back and forth across the layer, the input wavelet is returned with phase shifts in each frequency component caused by the particulars of the layer system. Thus, the input wavelet is “dispersed” in the geophysical signal processing sense [5]; the return is more spread out in time than the transmitted signal. By analyzing the duration over which the reflected energy ultimately returns relative to the duration of the transmit wavelet, we might infer the thickness of the layer. This will be pursued below primarily in relation to detection of near-surface buried objects, where the reflection is dominated by the R_0 component and the trailing energy betrays the buried target.

We devote most attention here to an alternative approach, the waveform recognition method. This attempts to go beyond previous work to recover some of the resolution lost in surveying at necessarily low frequencies. To apply the method,

one uses two things: 1) a set of reference waveforms for reflections from the layered system, from measurement or, as here, computed from a simple model; 2) correlations of these waveforms with those obtained in the data under study. The method performs a mathematical version of what one does by eye in the above figure, matching real and synthetic echoes that correspond to the same thickness. It rests on the expectation that every signal with finite energy correlates better with itself than it does with any other signal. Considering a given signal, one might suspect that strategic or coincidental exaggeration in an area of good match between it and another signal could produce a higher overall correlation value, despite lack of complete similarity in form. However, if the signals are properly scaled, then no matter how coincidentally large the local product is between their features, the highest peak in the correlation function will still be produced only by autocorrelation with zero shift.

To make this basis of our approach explicit, consider two signals $y(t)$ and $g(t)$. We assume that the two signals differ in form at least somewhere within the duration of significant activity. Each has a finite duration and, by appropriate scaling, has the same total energy, i.e. the same square integrated value. For convenience we take this value to be unity:

$$\int y(t)^2 dt = \int g(t)^2 dt = 1 \quad (1)$$

where the limits of integration are always large enough to catch all activity of interest in the signal. Because y and g are not the same, we may write

$$\int [y(t) - g(t)]^2 dt > 0 \quad (2)$$

Combining (1) and (2), we obtain

$$\int y(t) g(t) dt < 1 \quad (3)$$

This means that cross correlation (3) will always produce a smaller value than autocorrelation with zero shift (1).

In light of this we define our strategy. Given any subject radar record $y(t)$, we will seek a match against various candidates $g(d;t)$ from a reference set. The pre-computed reference set contains members corresponding to incrementally different pos-

sible layer systems (e.g. different d values), each of which is scaled so as to have unit energy in the sense of equation (1). We then determine the highest correlation value between $y(t)$ and all the $g(d;t)$. The best estimate of d is the value corresponding to that $g(d;t)$ that shows the highest correlation peak. That is, we assume that the highest correlation peak comes from autocorrelation with zero shift. While any number of other parameters can play the role of d , here it will usually correspond to layer thickness.

Expressed in equations: To analyze a given $y(t)$, form the correlation function $c(d;\tau)$

$$c(d;\tau) = \int g(d;t+\tau) y(t) dt \quad (4)$$

for each d . Place its maximum in $a(d)$

$$a(d) = \max_{\text{over } \tau} \{ c(d;\tau) \} \quad (5)$$

then

$$\max_{\text{over } d} \{ a(d) \} \Rightarrow \text{identifies best estimate of } d \quad (6)$$

This recitation of the computational sequence suggests the principal drawback of the system, namely that it involves multi-stage processing and can therefore be computation intensive: One may have to form a succession of $y(t)$ by windowing the record at successive locations in the neighborhood of significant activity; for each such windowing one must calculate (4) over a reasonable range of shifts, τ ; this is done over the whole range of relevant d values.

Layer Response and Transfer Functions

To proceed we need a reference set of $g(d;t)$ corresponding to reflections from a range of possible layer systems. Here these will be calculated, using a complex reflection coefficient for the combined layer-substrate structure, tantamount to a transfer function for the whole layer system together. While time domain discussion in terms of the R_i is sometimes clarifying, for the most part below we proceed in terms of such a frequency domain transfer function. Beyond its utility for calculating frequency dependent responses to any input, the particulars of the transfer function are

in themselves informative.

To calculate the transfer function, one solves for the fields in each medium and uses the results to determine an impedance transformation (e.g. [12], [13]), that is, the equivalent impedance of the entire layered system. Using this, we may write the frequency dependent complex reflection coefficient, $H_\ell(d; f)$, for the entire layer system as

$$H_\ell(d; f) = \frac{Z_1 - \eta_0}{Z_1 + \eta_0} \quad (7)$$

where Z_1 is the total impedance for the layer together with its semi-infinite substrate ,

$$Z_1(d; f) = \eta_1 \frac{\eta_2 \cos(kd) - i\eta_1 \sin(kd)}{\eta_1 \cos(kd) - i\eta_2 \sin(kd)}, \quad (8)$$

f represents frequency (Hz), η_m represents the impedance of the m^{th} layer (ohm), and i is the square root of minus one. Here and in what follows, we assume and suppress the negative exponent time factor $e^{-i\omega t}$. It is understood that the wavenumber k (m^{-1}) in (4) pertains to medium 1. $H_\ell(d; f)$ relates the normally impinging signal to the entirety of its reflected content from all depths. Hence it is, effectively, the layer system transfer function.

One may apply this single layer formulation recursively to describe a many layered system. Beginning at the bottom, the lowest (N^{th}) finite layer above a semi-infinite substrate forms a single layer system like that considered above. Z_N is given by (8) with appropriately shifted indices. Moving upwards layer by layer from the N^{th} one, at each i^{th} interface we may express the impedance up to that point in terms of the impedance of the current (i^{th}) layer and that of the entire system below it, Z_{i+1} (cf. [8], [13]):

$$Z_i = \eta_i \frac{Z_{i+1} \cos(kd)_i - i\eta_i \sin(kd)_i}{\eta_i \cos(kd)_i - iZ_{i+1} \sin(kd)_i} \quad (9)$$

In this scheme, Z_1 pertains to the entire system including and below the top layer, and it is used in (7) to obtain $H_\ell(d; f)$ for the whole system. In what follows, the combination of (7) and (9) provides the response of a layer with a dielectric constant that varies continuously across its depth. One approximates the continuous variation stepwise by subdividing the layer into many thin homogeneous

sections, each of which has a dielectric constant slightly different from its neighbors. Ideally, to preserve a facsimile of continuous variation at the scale of observation, the subdivision size should be much smaller than the local electromagnetic wavelength. At the same time, the divisions must not be so fine that insignificant dielectric contrast between layers produces negligible Fresnel coefficients at the subdivision interfaces. These constraints did not hamper the calculations described below in simulation of soil with continuous variation of moisture content.

Depending on the layer depth d , the reflection response $g(d; t)$ of the system to a monochromatic incident signal $s(t)$, with Fourier Transform $S(f)$, is

$$g(d; t) = \int H_\ell(d; f) S(f) e^{-2\pi i f t} df \quad (10)$$

where, again, we note that the negative time exponent applies. Thus, the overall reflection coefficient $H_\ell(d; f)$ serves as a transfer function, tantamount to the impulse response.

Examples of $H_\ell(d; f)$ appear in Figure 3 for an ice layer above other media. Here and elsewhere below we assume that the ice is lossless with a dielectric constant of 3.2. Each example substrate was assigned a real dielectric constant, equal to 88 for water at 0°C and 16 for the wet unfrozen soil. We note that for the greater dielectric contrast in the case with ice over water, the upper amplitude curve is somewhat flattened relative to the one pertaining to ice over unfrozen soil. In the extreme case of ice on a metal structure (perfect reflector, pec), the amplitude curve is completely flat at a value of unity (a lossy layer 1 material would show some of the oscillatory behavior in the other curves). In the sections below we examine the similarities and differences between these patterns and those in $H_\ell(d; f)$ for an electrically dense layer 1 and less dense medium 2. It has long been recognized that the typically oscillatory amplitude pattern might reveal the physical constitution of a layer system, e.g. reciprocally in the radiometric observation of layers of earth materials [14] or of thin layers of oil on water [15]. In principle this amplitude pattern could reveal oil slicks some millimeters in thickness. It would require micro- to millimeter wave frequencies, however,

which would not be useful for surveying the relatively impenetrable and rough surfaces of moist soil.

For the cases in Figure 3 we note that, despite large difference between the various amplitude patterns of $H_\ell(d; f)$, the phase pattern is relatively stable as medium 2 varies. The gross slope in the phase pattern reflects the fact that the principal return (R_1) is delayed, with further modulation evident in the curvature. This suggests that, if one tries to identify d by inferring the transfer function from measured data, it may be best to rely on the more stable phase pattern. We have done this successfully [9] by concentrating on the periodicity of the curvature pattern as opposed to its gross slope (delay). This strategy avoided errors associated with unknown and shifting time reference points in field records. At the same time, special measures were required to deal with thin ice conditions. A long lasting incident wavelet relative to the transmission time back and forth across the ice means that $H_\ell(d; f)$ is only obtained over a relatively small segment of the kd domain. Innovative techniques were required to infer the overall periodicity in phase pattern curvature of $H_\ell(d; f)$ when only a fraction of a period was available in the record. Overall, this is a difficult undertaking. Equivalently, in the time domain, when a long incident wavelet is convolved with the impulse response, it will produce overlapping counterparts to R_0 , R_1 , etc. Whatever the particular shape of the amplitude curves for $H_\ell(d; f)$ in the examples in Figure 3, we may rely on its phase content to accomplish shifts of $s(t)$ as shown in Figure 2. That is, as layer thickness increases, the R_0 and R_2 components will emerge respectively from the front and back of the R_1 response, and so forth.

In computational experiments using reference $g(d; t)$ based deliberately on various incorrect medium 2 dielectric constants, the time domain waveform recognition system outlined above in (4) through (6) still correctly identified layer thickness, as long as the layer (medium 1) dielectric constant assumed was accurate [10]. This means that the time domain processing implicitly responded to the crucial phase structure of $H_\ell(d; f)$ more than its widely varying amplitude pattern. While these computational experiments suggest

that the method is considerably robust, we must note a likely source of limitations. When one interface in a layered structure produces much stronger reflections than the others, then, somewhat inescapably, variations in the layer geometry will probably still produce reflections that feature this component most strongly. Especially in noisy data this may make it difficult to discriminate between different echoes that depend for their contrast on other, weaker R_i components. One may apply various remedial measures, as we do below, amplifying important portions of the signal that we know *a priori* should be of high important but diminished magnitude.

Dense Overlayers

To illuminate the phenomenology and provide a framework for discussion, we consider what may represent the densest naturally occurring layer over a much less dense basement, namely water on ice. In airborne field surveying near the end of winter, we have observed very bright returns from wet ice surfaces. Virtually no information came through from beneath the surface. This was the case even when the water layer on the ice seemed very thin. To illuminate this situation we construct the transfer function for a layer system like that previously considered, but with a high, complex value for medium 1 and lossless ice in the semi-infinite medium 2. The water's dielectric constant is frequency dependent and can be expressed as

$$\kappa = \kappa_\infty + \frac{\kappa_s - \kappa_\infty}{1 - i\omega\tau_r} + i\frac{\sigma}{\omega\epsilon_0} \quad (11)$$

where the unitless dielectric constant κ depends on the static value κ_s (88.3 at 0°C), the high frequency value κ_∞ (5.28), the permittivity of free space ϵ_0 (F/m), the angular frequency ω (s⁻¹), the dc conductivity σ (S/m), and the relaxation time τ_r (s). In our frequency range, dielectric relaxation is generally the major loss mechanism. The temperature dependence of τ_r introduces temperature dependence into κ ; at 0° C τ_r is equal to about 1.8×10^{-11} seconds (e.g. [16]). Liquid water at its freezing temperature and at room temperature differ little in lossiness below about 100 MHz, with attenuation somewhat less than 2 dB/m. However, the lossiness and temperature sensitivity due to τ_r rise steeply as frequency increases. If we assume

typical water conductivity of 0.01 S/m, then at 1 GHz the room temperature attenuation rate is about 35 dB/m, while that for freezing temperature water is almost 60 dB/m greater. Thus, using shorter, higher frequency wavelets to increase resolution brings severe penalties in terms of lossiness for wet media.

The effect of lossiness is illustrated in Figure 4, for a hypothetical 3.5 cm deep water layer on ice. In addition to curves based on the aforementioned values of σ and τ_r , the dashed lines show values for an equivalent lossless water layer ($\sigma = 0 = \tau_r$). Numbers on the upper horizontal axis indicate values of $k_R d$, where k_R is the value of the real part of the wavenumber of the water. Virtually all discernible pattern disappears in the lossy case as frequency increases past 1 GHz.

In what has preceded, we have examined the effects of the layer system transfer function pattern for *reflection* of input and considered how we might infer that transfer function, in effect. However, if we are interested in seeing through the wet layer, we must consider *transmission* through the two interfaces, each way. One may easily solve for fields in the three zones to obtain an air through water to ice transmission coefficient T_{02} equal to

$$T_{02} = \frac{T_{01}T_{12}e^{ikd}}{1 + G_{01}G_{12}e^{2ikd}},$$

$$G_{jm} = \frac{\eta_m - \eta_j}{\eta_m + \eta_j}, \quad T_{jm} = \frac{2\eta_m}{\eta_m + \eta_j} \quad (12)$$

where as before it is understood that $k = k_j$ and all parameters are complex. G_{jm} and T_{jm} are the interfacial Fresnel reflection and transmission coefficients for a wave impinging on the m^{th} from the j^{th} layer. For detecting objects or interfaces below the surface of the ice, we must apply an additional transmission factor for the ice-water-air return path. The result is a round trip transmission coefficient T_{ret}

$$T_{ret} = T_{02}T_{20} = \frac{\eta_0}{\eta_2} T_{02}^2 \quad (13)$$

While all factors are frequency dependent, it is primarily k_j in the exponential factor in the numerator of (12) that produces the dramatic lossiness effect in T_{ret} as frequency increases. Figure 5 (top) illustrates this for the same 3.5 cm layer.

A few things are immediately striking from these figures. Very little relative phase shifting occurs between the reflection components (Figure 4, bottom); the surface R_0 reflection dominates. Some curvature occurs in the phase pattern, such as might be analyzed for thin layers by the method of Riek et al. [9]. However, when lossiness suppresses the R_1 return at higher frequencies, very little of this phase pattern is evident near or above 1 GHz. Similarly, the amplitude pattern flattens out as frequency increases, ultimately becoming a barely modulated undulation about the value of the reflection coefficient for water alone. Perhaps the most notable insight from these plots is the recognition that the magnitude of the reflection (amplitude curve) over much of the frequency range is *greater* than the ~ 0.8 coefficient value for water alone (Figure 4, top). Correspondingly, in Figure 5 (top) *both* lossy and lossless curves show a large suppression of $|T_{ret}|$ in the trough below about 500 MHz. Both curves show this reduction because it is not due to material lossiness but rather to destructive interference of the interface echoes. The valleys in the curves represent 20 dB diminution of returns from within the ice, even at quite low frequencies where we expect minimal losses based on absorption.

This layer effect presents special problems as we try to see things within the ice below a water layer. Because of loss mechanisms, the wavenumber k_j is not linearly proportional to frequency, though the real part is approximately so. Different frequency ranges produce different degrees of loss, so that overall the curves do not scale precisely as a function of $k_R d$. Nevertheless, scaling applies sufficiently to make our point: Increasing bandwidth into higher frequencies or restricting applications to larger d values, in the hope of achieving tolerable resolution, is a largely futile strategy. In graphical terms, reaching for increased k or d range would increase the number of cycles in figures like 4 and 5. However, the discernible pattern would all be compacted against the left side of the graphs. Most of the expanded kd range would feature only the barely modulated curves, of the sort on the right sides of the graphs in Figure 4 and 5 (top). That is, returns will not be very distinguishable from what a water surface alone would produce. If we restrict ourselves to cases with thin water layers, in effect we constrain our-

selves to the first cycle of the pattern. Ideally we must restrict ourselves to thicknesses small enough so that our kd range runs from the left side of Figure 5 (top) to some point short of the bottom of the first valley. Figure 5 (bottom) shows $|T_{ret}|$ vs. frequency for two different small values of d . These curves are essentially stretched out renditions of the first half cycle in the upper Figure 5. Also shown is the amplitude spectrum of the wavelet from our GSSI 101C antenna. We see that the two layer thicknesses chosen, 0.35 mm and 3.5 mm, roughly bracket the transition between probability and improbability of sensing things within the ice. Even using our antenna with a center frequency around 500 to 600 MHz, one would suffer considerable reduction in signal with a covering water layer 3.5 mm deep. One can use Figure 5 to project approximate frequency limits for deeper water layers: To be confident about receiving reflections from within the ice as water thickness approaches 1 cm, the frequency range would have to be restricted to within the first couple of hundred MHz.

These considerations will be applied to other observations in the literature, where one sees diminution of returns as a surface water layer over ice increases in thickness up to 1 cm. Through the perspective above we argue below that, somewhat counter-intuitively, a further increase in water layer thickness would have shown *increased* visibility of the interface below the ice.

RESULTS

On Thin Ice

The waveform recognition method was applied over a range of ice thicknesses under different conditions, with the reference $g(d;t)$ set of possible echoes calculated using the transfer function system set forth above. In the first case, ice was grown on top of a large foil sheet in a laboratory setting (details in [10]). Figure 6 (top) compares measured thicknesses of the ice with those obtained using our signal processing system on the radar returns. Clearly the resolution is quite good. With a duration of about 4 ns (Figure 2), the length of the wavelet within the ice approaches 70 cm. Nevertheless, the method distinguishes a layer as thin as about 4 cm from the no-ice case and distin-

guishes successfully between layers that differ by only about 1 cm in thickness. In this case, medium 2 is a perfect reflector; there is no amplitude modulation, i.e. the pattern of $|H_t(d; f)|$ is flat (see Figure 3, top). All results devolve from implicit detection of wavelet dispersion due to phase shifting. A processing approach relying on this appears to be remarkably robust.

Figure 6 (bottom) shows similar measurements and calculations for ice that grew under natural winter conditions on an outdoor pond at the U.S. Army Cold Regions Research and Engineering Laboratory (CRREL), in Hanover, NH. The data processing system was the same as in the previous example, except that the candidate $g(d;t)$ set was based on a substrate of cold water instead of foil. Here again we note very good agreement. While the slight disagreement at greater ice thickness for the laboratory ice case is unexplained, we trace it here to a distortion of the R_1 return. This may be due to contamination of the ice in the form of grit and possible unfrozen water, producing dispersion and a slightly higher effective dielectric constant than was assumed in the processing. In any case, the slight errors are less noteworthy than a feature of the processing system that allows one to assess the reliability of results in the absence of ground truth. The value of $a(d)$, that is, the peak correlation value that indicated the best match, is shown next to each plotted point. Given the energy scaling employed, a perfect match would produce a value of unity. We note that, where agreement is best, the maximum correlation values are near unity, while they drop elsewhere in proportion to the divergence between measured and calculated results.

Open Lead in a River

Radar surveying of river ice was done from a helicopter with antennas mounted on the skids, in the manner described in [10] and [17]. Figure 7 shows an open lead at a location in the Yukon River, which was traversed by a surveying transect line, for which field data were provided [18]. The figure also shows wiggle plots of signals from the record, together with the corresponding thickness profile computed by the same signal processing system as above. We note that the processing system distinguishes the zero thickness over the open water, at the left of the figure. It provides a con-

tinuous thickness profile over ice sections that both are and are not thick enough to separate the R_0 , R_1 , R_2 etc returns. Of course, more than anything else, the processing system indicates a best estimate of delay across the layer, not thickness per se. The “knob” of ice at the edge of the open water is often observed at the edge of such open leads, containing possibly congealed frazile ice buildup below the surface [17]. Thus, our processing faithfully indicates this buildup but may not provide accurate thickness information if some unfrozen water content makes the dielectric constant uncertain. Rather than estimate based on any particular dielectric constant estimate, the figure simply shows the shape of the delay profile. The dip in the profile near the right side seems to indicate a disordered ice configuration, rather than a real diminution of thickness in that locale. The layer may contain unfrozen water and chunks of ice at depth, producing multiple reflections. While the duration of significant activity in the signal at this point is comparable to or greater than that where the ice is thick, the processing system attests that it does not resemble the thick ice reflections in form. Its shape in early time resembles the returns from clear layers nearby, followed by strong trailing content. One can judge the reliability of processing in this locale by examining a corresponding profile of correlation maxima (e.g. numbers on Figure 6, bottom). In any case, the method has succeeded in producing a generally credible profile for this field case, without gaps over important areas where the ice is too thin to resolve with traditional pulse timing methods.

Dense Surface Layers: Wet Ice

Interpreting some previous results in light of the discussion above can suggest some counter-intuitive results. Arcone [19] discusses surveying of wet, dry, and partially thawed river ice. In some of his field measurements on wet but otherwise intact ice, a consistent ice bottom interfacial reflection appears, in measurements with a 500 MHz center frequency system. However, these reflections from within (below) the ice are diminished by roughly one third relative to the top surface reflection, in comparison to ice with no surface water layer. Further, Arcone calculates theoretical echo sequences for a water layer on top of ice, with river water below the ice, for the same 500

MHz center frequency wavelet. The computed scans show first a reflection from the top water layer and its two interfaces, followed in time by a reflection from the ice/river water interface below. For one or two mm of covering water depth, the ice top and bottom reflections are comparable in magnitude. As the assumed covering water depth is increased, the reflection from the ice bottom steadily diminishes. As the assumed surface water depth reaches 1 cm, the lower ice bottom/ river water reflection is barely perceptible. This may be interpreted in terms of the curves in Figure 5 (top). We focus on the first cycle, which contains a peak near the origin, followed by a valley, followed by the first peak to the right of the valley at around 450 MHz for our 3.5 cm thick surface water layer. If one translates this into $k_R d$, the first peak to the right of the first valley is at about $k_R d = 3$. Calculating k_R from the center frequency of 500 MHz, we see that Arcone’s example covering water layers produce responses beginning near the origin (left side of the figure) for the thinnest water layers and ending at $d = 1$ cm near the bottom of the first valley in $|T_{ret}|$. That is, theoretically, further increases in d should actually show an *increase* in the ice bottom/ river water return, at a level somewhere between the lossy and lossless curves in the upper Figure 5.

Dense Surface Layers: Thawing Soil

The method was also applied to detecting and characterizing the surface thaw layer on an experimental dirt roadway surface. The soil was a silty loam, nearly saturated before freezing, with enough fine grain content to hold the moisture well. This means that for the relatively thin thaw layers of interest (5–15 cm), the moisture content was approximately constant over the thaw layer depth. The soil conditions provided a good representation of a typically moist dirt road during spring thaw. The question was whether, at this high moisture content, the lossiness was so great that one would not detect the influence of the R_1 return, mixing distinctively with the larger R_0 reflection.

The measurements were taken at CRREL’s Frost Effects Research Facility. One end of the approximately 35 m long test section was somewhat warmer than the other, so that the thaw depth at the warm end was about 9 to 10 cm, while at the colder end it was about half that. These were good

test conditions because the depths were great enough to be significant and to show some effect on the radar record; they were shallow enough so that radar penetration might be sufficient; and they were in a critical range relative to vehicle tire traction and motion resistance ([2]-[4]). When thaw depths were measured by taking soil cores at approximately 5 m intervals along the longitudinal measurement transect, volumetric moisture content data were also obtained. A single value was obtained for the whole depth from each sample, with values reliably about 0.3 ± 0.01 . From this, a value of about 17 for the real part of the soil dielectric constant, κ_{sR} , was inferred from the relationships provided by Topp et al. [20].

The imaginary part of the soil dielectric constant, κ_{sI} , is due essentially entirely to the liquid water. Its value was estimated by assuming that the dielectric constant of the soil when completely dry was about 3.2. The difference between that value and the κ_{sR} obtained from Topp et al. at any given moisture content was considered to be due to the presence of water. The size of this difference was determined relative to the real part of the dielectric constant of water alone. It was then assumed that the water contributed the same proportion of its imaginary part to κ_{sI} as it contributed from its real part to κ_{sR} . At each frequency within the band used, equation (11) provided the complex dielectric constant of the water, assuming a temperature of 0°C and the values of σ and τ_r cited above. This strategy produced reasonable values of κ_{sI} relative to those shown by Hoekstra and Delaney [21] and Arcone and Delaney [22]. Also, the value shown by Hoekstra and Delaney and the values calculated here suggest that, at the 500 to 600 GHz center frequency of the antenna used, loss for the R_1 return across the deepest layer may only be about 15%. The relatively modest attenuation at these lower frequencies argued for restricting measurements to the GSSI 3102 antenna, despite some loss of resolution relative to our higher frequency radars. Slight attenuation of the R_1 return also meant that some inaccuracy in the approximation of κ_{sI} would not introduce significant error.

Figure 8 shows the transfer function calculated for the approximate maximum thaw depth, using the above calculation of the dielectric constant. The figure suggests that the measurements reside

in a low enough frequency range so that lossiness should not too greatly suppress the characteristic patterns caused by interacting interface echoes. This would not be the case in the range at the right end of the figure. The 9 cm depth represents the worst case considered from the point of view of diminished R_1 return, while providing the best separation that we may expect between the R_0 and R_1 echoes. Still, the separation is not very great, as shown in the middle portion of Figure 8. The zero thickness (no layer) echo was derived from the reference transmit wavelet. The figure shows that the difference between it and the 9 cm layer echo lies only in some trailing content, which has been amplified substantially. The bottom of the figure shows the temporal weighting measure employed to amplify that trailing content relative to the stronger early time R_0 portion by a factor of 4.

Figure 9 shows thaw depths along the test section, as obtained from the soil cores and other manually invasive measures and from the processing of the radar records. Agreement is quite striking, even at the shallow end of the roadway, where we may expect less trailing content than is visible in Figure 8 (middle). Also to be noted are the many false zero thickness values obtained from the processing. As mentioned above, most returns with one strongly reflecting interface are likely to correlate well with the zero thickness candidate. Under our less than optimal test conditions, the trailing content had to compete with a considerable amount of noise, due partly to multiple reflections between the antenna and ground surface. Under better conditions, including higher antenna elevation, this might be improved. Most important, whenever the noise level was low enough so that meaningful trailing content had an impact, the processing system identified depths in the right range. There is virtually no scatter between the false zero depths and those near the measured values.

Simulation Experiments: Generalization to Soil Moisture Content per Unit Area

Here we examine the results of two simulation experiments. For the first, we note that the reference set of echoes $g(d;t)$ can be constructed for other functional dependencies in the role of d . In this case we replace d with moisture content per unit area of thawed ground, $\Theta_v d$, where Θ_v is

volumetric moisture content. In the second simulation experiment, treated in the next section, we address cases with continuous variation of moisture content in the surface soil, as opposed to the sort of abrupt layering considered here and above.

The simulation work reported in this section is designed to test the generality of the waveform identification method in application to wet surface soil layers. It illuminates the meaning of the quantities provided by this sort of radar record processing for a moist soil layer. The exact form of the interference pattern produced by the succession of two interfaces depends on the dielectric constants of media 1 and 2 for a given layer thickness. Still, for a wide range of thicknesses and moisture contents, we may obtain a good first approximation of the pattern from a gross estimate of the attenuation and especially of the delay, i.e. transmission time across the layer, applicable within our frequency band. The approximate delay provides a gross estimate of the phase shifting, as seen in the various transfer function phase patterns displayed above. This delay is approximately proportional to $\text{Re}\{\sqrt{\kappa}\}d$. For our purposes in what follows, we will consider the square root of the real part of κ to be a reasonable approximation of the real part of the square root. Now, examining the relationships provided by Topp et al. [20], we note that the real part of κ for soil bears a nonlinear relationship to volumetric moisture content, Θ_v . In particular, if the soil is not too dry, the real part of κ might be described roughly as proportional to the square of Θ_v (cf. the regression fits that Topp et al provide to their data). Altogether, this means that we may approximate the delay across the layer as linearly proportional to the product $\Theta_v d$. This is the moisture content in the layer per unit area of soil surface.

Knowing the quantity $\Theta_v d$ should often be valuable in itself. In any case, working terms of $\Theta_v d$ allows us to generalize the processing system. To illustrate this, we perform a test in which we construct a number of synthetic radar returns from thawed soil layers, using the methods described above. We choose layer Θ_v values of 0.15, 0.25, 0.35, and 0.45, together with d values of 7, 12, and 17 cm. Combining these in all possible combinations, we obtain twelve contrasting cases. For each case, we will analyze the synthetic records using a reference set of candidate matching sig-

nals obtained for a range of thicknesses from zero to 30 cm, using a single Θ_v value of 0.3. Thus none of the synthetic returns comes from a layer system whose characteristics coincide with the members of the reference set. Both the synthetic returns and the candidates for matching are classified in terms of the $\Theta_v d$ values that pertain to each. We then perform the same correlation processing as described above, to see which candidate $g(\Theta_v d; t)$ (and hence, which $\Theta_v d$ value) matches best with each synthetic record.

Figure 10 shows the results, comparing $\Theta_v d$ values calculated from the radar processing of each synthetic record with those used to construct the synthetic returns (the “actual” values). We note that, despite the wide variation of Θ_v and d values, and despite the difference in character between the layers analyzed and those producing the reference set for matching, we have predicted $\Theta_v d$ values in the synthetic echoes quite well. This suggests two things: First, that we may proceed in this sort of processing using a single, or at most a few, representative libraries of candidates for matching. We need not be concerned about having candidates based on an accurate moisture content, which we may not know. We can still extract what is tantamount to the approximate delay (and attenuation) across the layer. Second, having obtained a value of $\Theta_v d$ from the signal processing, we can estimate either of the two factors in the product, given an estimate of the other.

Simulation Experiments: Continuous Gradient of Moisture Content

The second simulation experiment treats soil layers for which we may not assume that the moisture content is vertically uniform. Because the layers in the previous sections were relatively thin and the soil had some fine grain content, it was reasonable to assume an approximately constant Θ_v across the depth. However, when the unfrozen soil is sufficiently deep, this will not be the case, especially for soils of mixed type. In general, proceeding downwards from the surface of a drying unfrozen soil, we pass through a vadose zone in which saturation increases with depth. It reaches a maximum at some point above the water table. The height of that point above the water table, i.e. the capillary rise, and the depth over which the

transition from surface to deep (maximum) moisture content takes place both depend upon the soil type. Figure 11 (top) illustrates this. We may express the volumetric moisture content as a function of depth in this situation using the applicable soil moisture characteristic curve ([23, 24]). These curves have certain characteristic shapes; here we apply the widely used form advanced by van Genuchten, with parameters chosen for convenience of the test. Basically, the assumed conditions produce a transition from surface to deep moisture content over twice the depth for the hypothetical finer grained soil as for the coarser soil. One may calculate the transfer function H_v for this soil system using the recursive multi-layer method (equations 7–9). Numerical solution of the Riccati equation for some parallel cases verified the method, with soil k estimated as above for each moisture content and frequency.

The lower plot in Figure 11 shows what might be obtained from broadband surveying of such soil systems from an elevated platform. The amplitude of H_v shows a low frequency peak with a magnitude approximately equal to that of the reflection coefficient for a uniform soil at the deep moisture content. As frequency increases, $|H_v|$ approaches a limit around the value of the reflection coefficient for uniform soil at the dry surface moisture content. These limiting reflection coefficient values imply soil k values, which in turn imply moisture contents (e.g. via the formulae of Topp et al. [20]). The frequency width of the transition between the low and high frequency limits is inversely proportional to the depth over which the moisture content transition takes place. Numerous other numerical experiments showed that the precise shape of the moisture transition does not have a significant influence on this picture. Basically, the very long wavelengths see the transition from air to the deep moisture content as sharp. It is as if they reflect from a sharp boundary between air and soil at the deep moisture content. The high frequencies reflect from the ground surface and fail to penetrate very far in any case. In addition, the subsurface moisture gradient appears smooth on their scale and therefore stimulates little reflection. In practice, for more realistic fine grained soils the vadose zone would often be spread over a greater depth, and quite low frequency GPR sys-

tems would have to be used to gain information over the relevant band. Nevertheless, this simulation experiment suggests that broadband, low frequency surveying might be able to reveal surface and deep moisture contents, as well as an approximate depth over which the transition takes place between the surface and deep values.

Buried Objects

In this section we report results of applying the above methods to detection of buried metallic objects. In particular, cases were considered in which reflections from the objects could not be separated in time from reflections from the ground surface. This may occur when objects are buried even 10 or 20 cm deep in moist soil, when one resorts to frequencies low enough to penetrate moist soil, especially from an elevated antenna. In the first test, a waveform recognition approach was applied, with the soil layer consisting of the material between the top of the (perfectly reflecting) target and the soil surface. Measurements were taken over two buried targets: a truck brake drum, generally resembling an anti-tank mine in size and shape, with concentric ridges and crenelations; and a metallic six inch (~15 cm diameter) training mine. These were both buried at a 10 cm depth in moist silty soil. A 500 to 600 MHz center frequency wavelet antenna was used, being about the highest frequency signal that might still penetrate to the target depth. The reference set of $g(d;t)$ was based on this wavelet, assuming merely that the target reflected about 17% of the incident signal, based roughly on the ratio of target size to beam width. Thus, an extremely crude, flat lower interface model was applied, taking no account of detailed target structure.

Figure 12 shows results in terms of $a(d)$ curves. That is, the figure displays peak correlation values of the theoretical $g(d;t)$ waveforms when matched against measured reflections, as a function possible depth of target, d . The top curve in the upper figure shows that the system finds essentially 100% correlation between a reflection from the ground surface alone and a reference wavelet (i.e. the $g(d;t)$ corresponding to zero depth as the source of the reflection). When either the anti-tank mine model or the 15 cm training mine is buried below the surface, we note that the cor-

relation with a zero-depth reflection is much lower, and there is a strong peak corresponding to the $g(d;t)$ for a target at about the correct depth. Thus the system distinguishes clearly between cases with surface reflection only and cases with buried metallic reflectors on the basis of waveform characteristics, even when the surface and object reflections cannot be separated in time. We note that, in these case and that treated below, the presence of a target could not be inferred from greater magnitude of the reflections over the target. The target failed to increase the peak reflection magnitude, which was dominated by the ground surface. The target manifested itself only in a change in the form and duration of the surface reflection.

Finally, we consider object detection using a measure of wavelet distention in time, i.e. wavelet dispersion. The technique relies on very gross features of waveform alteration caused by the near surface buried object without resorting even to a model as crude as that applied in the tests above. In particular, it takes advantage of the sort of spread in signal caused by overlapping reflections, as illustrated in the introductory discussion above (Figure 2). However, in this case the R_o surface reflection is much stronger than the trailing R_l component from the target. Along with other measures, the signal processing applies variable gain to reduce the R_o reflection in early time, and amplify the much weaker trailing content, as per Figure 8 (bottom). Squaring, smoothing, and integrating the signal provides a continuous, monotonic record of cumulative energy arrival over time, as shown at the top of Figure 13. Here the two buried targets are the 15 cm training mine and a car alternator, similar to more geometrically elaborate mines in size, complexity, and style of protruding features. These targets were buried in the same wet soil as above, such that, with the same antenna, ground surface and target reflections overlap greatly. When the reflection comes only from the ground surface, with miscellaneous surface roughness and subsurface clutter, energy arrives in accordance with the solid line on the left of the upper figure. Whether the subsurface target is the practice mine or the alternator, we note quite similar delays in cumulative energy arrival, both contrasting with the no-target case. Using the time point at which 85% of the energy arrives as a measure, the cases with tar-

get show almost a factor of 2 increase in trailing energy arrival time, given the same variable gain applied to both target and no-target cases.

The bottom portion of Figure 13 shows results from the same wavelet dispersion measure system, applied to a case with the anti-tank mine model buried at a depth of about 14 cm in very wet clayey soil. At this depth, with very high moisture content, reflections from the target still overlap very much with surface response. Wet soil with a significant clay size fraction has contributed substantially to the failure of ground penetrating radar in field tests of systems for detecting subsurface ordnance. In this test, a 400 MHz center frequency antenna was moved through positions from left to right in the figure, with the target buried below the positions on the left but not on the right. When the soil is unfrozen, the surface reflections and loss through the soil are so severe that there is no detectable wavelet distention in the return from the surface, even with amplification of the trailing content. However, when the clay is frozen, this system clearly identifies the presence of the target, with approximately a factor of 2 increase in the 85% energy arrival time. The protrusion in the curve for the frozen case between positions 24 and 32 reflects the presence of a hyperbolic trace, as incidence on and reflection from the target is increasingly oblique. Such hyperbolas are commonly seen in plots of signal over time vs horizontal location, when there is an isolated target. In this case, however, the hyperbola is partly merged with the ground surface reflection. We expect results similar to these when dry (as opposed to frozen fine grained) soil is considered.

SUMMARY AND CONCLUSION

The primary method described above, using waveform recognition, proved itself to be robust, flexible, and accurate, when one has a reasonably well defined transmit wavelet to work with. Thus, it applies best to surface layers and buried objects sensed from an elevated antenna. Most often in the applications reported here, layer thickness was the characteristic identified by the system. It appears that the method can instead identify volumetric moisture content per unit area (average

volumetric moisture content times wet layer thickness) when applied to thawing soil. It should apply similarly to a moist layer behind a distinct wetting front above dry soil.

While the method can be applied successfully to layers of any thickness, it is particularly advantageous for treating layers that are thin relative to the incident wavelength or incident pulse. That is, one gains the most with this approach when interface separations are small enough to produce echoes that overlap. For instances with a less dense layer over a denser substrate, the method was tested on lab and pond ice, demonstrating its ability to discriminate very thin layers when relatively low frequencies must be employed. The method distinguishes a no-ice condition from an ice layer 4 cm thick and correctly distinguishes thicker layers from one another when they differ in thickness by only about 1 cm. This was accomplished using UHF pulses with center frequency wavelengths of about 20 cm in ice, with a pulse length in ice between about 55 and 70 cm. Against field data the method also produced reasonable ice profiles near an open lead in river ice. Without gaps over thin sections the system indicated likely subsurface buildups and thinning down near the water's edge.

For electrically dense layers over less dense substrates, the analysis suggests that layering effects may hinder the surveying of wet ice much more than one would expect based on the inherent lossiness or sheer reflectivity of the surface wetness. A round trip transfer function, for signals passing through the water into the ice and back, shows strong and broad cyclical minima, regardless of medium lossiness. In typical GPR frequency ranges, much of the essential band may be suppressed because it resides near the bottom of the first minimum. Thicker water layers may take one beyond this first cyclical minimum in the transfer function but then entail greater overall signal loss due to absorption in the water. Referring the transfer function pattern to some cases discussed in the literature, we argue that *thicker* layers of water on top of wet ice may have yielded *stronger* returns than were observed from the ice bottom. This is due to the second cycle of constructive interference between the reflections from the layers successive interfaces. In transfer function terms, it is

because of the second, higher frequency maximum in the round trip transfer function, which is still likely to be a strong peak despite lossiness in the water.

For thawing soil the method proved successful in detecting quite thin surface layers relative to incident wavelength, within a range of thaw depths that is critical for vehicular trafficability considerations. This is important because it allows one to use low enough frequencies to penetrate the wet soil without such loss of resolution that the surface layer cannot be distinguished. In completely unfrozen soils, field conditions may feature vadose zones with continuous variation of soil moisture content from low values on the surface to high values at depth, without the presence of abrupt layering. Simulations suggest that broadband surveying from elevated platforms at UHF and lower frequencies may succeed in identifying the contrasting surface and deep moisture contents, together with the approximate depth over which the transition from one to the other takes place. Such determinations would offer significant advances in remote sensing of soil conditions for agricultural and environmental monitoring purposes.

Using quite a simple model to produce the necessary set of reference echoes, the waveform recognition approach successfully identified cases with buried metallic targets, when reflections from the subsurface targets could not be separated in time from the ground surface return. The system also provided correct depths to the targets. We note that, in these cases, the presence of near-surface targets would not have been evident from greater amplitude in the overlapping soil surface and target reflections. Rather, it is the form and duration of the combined surface plus target echoes that offer distinctive patterns. By identifying characteristic distortions in time of combined surface and target reflections, a second simpler method of detecting near-surface buried targets is proposed. This method does not depend on details of the waveforms. Based on the temporal trajectory of returning energy, the simpler method succeeds in exposing the presence of a mine-like target in frozen soil. When the same wet clayey soil is unfrozen, the target cannot be distinguished. We expect the same relative success for this method when

such soil is dry, as opposed to frozen.

REFERENCES

1. Ashton, G.D. (1986). River and Lake Ice Engineering, Water Resources Publ., Littleton, CO, 504 pp.
2. Shoop, S.A. (1990). Mechanisms controlling vehicle mobility on a thawing soil, Proc. 10th Intl. Conf. ISTVS, Kobe, Japan, 301-311.
3. _____ (1993a). Thawing soil strength measurements for predicting vehicle performance, J. Terramech., vol 30, 405-418.
4. _____ (1993b). Effect of soil thaw on off-road vehicle traction, Proc. 6th Intl. Conf. Permafrost, Beijing, 559-563.
5. Robinson, E.A. and S. Treitel (1980). Geophysical Signal Processing, Prentice-Hall, Inc., Englewood Cliffs NJ, 466 pp.
6. Mendel, J.M. (1983). Optimal Seismic Deconvolution, Academic Press, 254 pp.
7. Rossiter, J.R., D.W. Strangway, A.P. Annan, R.D. Watts, and J.D. Redman (1975). Detection of thin layers by radio interferometry, Geophys., vol 40, 299-308.
8. Parchomchuk, P., W.W. Wallender, and R.J. King (1989). Direct solution for dielectric properties of a lossy two-layered material, IEEE Trans. Geosci. Rem. Sens., vol 27, 310-315.
9. Riek, L., R.K. Crane, and K. O'Neill (1990). A signal-processing algorithm for the extraction of thin freshwater-ice thickness from short pulse radar data, IEEE Trans. Geosci. Remote Sens., vol 28, 137-145.
10. O'Neill, K. and S.A. Arcone (1991). Investigations of Freshwater and Ice Surveying using Short-pulse Radar, CRREL Report 91-15.
11. Davis, J.L. and A.P. Annan (1989). Ground-penetrating radar for high-resolution mapping of soil and rock stratigraphy, Geophys. Prosp., vol 37, 531-551.
12. Cheng, D.K. (1989). Field and Wave Electromagnetics, Addison-Wesley, 720 pp.
13. Wait, J.R. (1981). Wave Propagation Theory, New York: Pergamon.
14. Blinn, J.C. III, J.E. Conel, and J.G. Quade (1972). Microwave emission from geological materials: observations of interference effects. J. Geophys. Res., vol 77, 4366-4378.
15. Skou, N. (1986). Microwave radiometry for oil pollution monitoring, measurements, and systems, IEEE Trans. Geosci. Rem. Sens., vol 24, 360-367.
16. Stogryn, A. and G.J. Desargant (1985). The dielectric properties of brine in sea ice at microwave frequencies, IEEE Trans. Ant. Propagat., vol AP-33, 523-532.
17. Arcone, S.A. and A.J. Delaney (1987). Airborne river-ice profiling with helicopter-borne UHF short-pulse radar, J. Glaciol., vol 33, 1-11.
18. S.A. Arcone, personal communication.
19. Arcone, S.A. (1991). Dielectric constant and layer-thickness interpretation of helicopter borne short-pulse radar waveforms reflected from wet and dry river-ice sheets, IEEE Trans. Geosci. Rem. Sens., vol 29, 768-777.
20. Topp, G.C, J.L. Davis, and A.P. Annan (1980). Electromagnetic determination of soil water content: measurements in coaxial transmission lines, Water. Resour. Res., vol 16, 574-582.
21. Hoekstra, P., and A. Delaney (1974). Dielectric properties of soils at UHF and microwave frequencies, JGR, vol 79, 1699-1708.
22. Arcone, S.A. and A. J. Delaney (1982). Dielectric properties of thawed active layers overlying permafrost using radar at VHF, Radio Sci., vol 17, 618-626.

23. Bumb, A.C., C.L. Murphy, and L.G. Everett (1992). A comparison of three functional forms for representing soil moisture characteristics, *Ground Wat.*, vol 30, 177-185.

24. van Genuchten, M. Th. (1980). A closed-form equation for predicting the hydraulic conductivity of unsaturated soils, *Soil Sci. Soc. Am. J.*, vol 44, 892-898.

Figure 1. Impulse response of a layer with semi-infinite substrate, illustrated by schematic time sequences for lossless media. The incident signal impinges from the air above the layer and returns in multiple reflections (R_i) from the two interfaces, with different sequences appearing for two cases: water over ice, and ice over water.

Figure 2. Real and synthetic waveforms for reflections from ice over foil: transmit wavelet (a); synthetic (b) and real (c) echo from approximately 7 cm thick ice sheet; synthetic (d) and real (e) echo from approximately 17 cm thick ice sheet; synthetic echo from 24 cm thick ice sheet (f).

Figure 3. Impulse responses illustrated in the frequency domain for a layer of ice over moist unfrozen soil, over water, and over a perfect electrical conductor (pec).

Figure 4. Amplitude (top) and phase (bottom) of transfer function for a 3.5 cm thick water layer on top of semi-infinite ice. Dashed lines show patterns that would apply if water were lossless; k_R is real part of k_I .

Figure 5. Top: $|T_{ret}|$ as a function of frequency, for lossy and lossless water layer 3.5 cm thick, on top of ice. Bottom: $|T_{ret}|$ vs frequency for thinner lossy water layers, shown relative to the spectrum $|S|$ of a surveying wavelet.

Figure 6. Top: Comparison of thickness determinations for an ice sheet over foil, from direct measurement and from calculations using radar echoes with the signal processing system; Bottom: same for pond ice. Points show data, dashed line is locus of perfect agreement.

Figure 7. Open lead in river ice, with reflected radar signals and corresponding thickness/delay profile determined by the signal processing algorithm.

Figure 8. Top: Transfer function for a 9 cm thick thawed soil layer with a volumetric moisture content of 0.3. Middle: Temporally scaled versions of

the reflection from a foil sheet (0 cm thickness layer), used to construct the transmit wavelet, and of the reflection from a 9 cm thick thaw layer. Bottom: temporal scaling factor used in the middle figure and in all signal processing for the thaw layer.

Figure 9. Thaw layer thicknesses along the thawing dirt roadway, as determined by direct measurement and by signal processing of the radar returns.

Figure 10. Comparison of “actual” $\Theta_v d$ values and those calculated from radar signal processing for a matrix of synthetic cases with different layer depths and moisture contents.

Figure 11. Top: Moisture content profiles between water table ($h = 0$) and soil surface for two hypothetical soil types, where the water table lies 20 cm below the ground surface for the coarse soil, and 40 cm below it for the finer grained soil. The relevant transition (vadose) zone widths are 10 and 20 cm, respectively.

Bottom: Transfer function amplitude for the two unsaturated soil profiles, also showing reflection coefficient values for uniform soil at the surface (“top”) and at the deep subsurface (“bottom”) moisture contents.

Figure 12. Top: Maximum correlation values as a function of possible target depth for measurements over ground surface only (no target) and over the buried brake drum; and (bottom) over the 15 cm mine, also buried at 10 cm in moist silty soil.

Figure 13. Top: Cumulative energy arrival C as a function of time point N , for reflections from ground surface alone and from surfaces with shallow targets below. Bottom: Measured durations of 85% cumulative energy arrival when antenna passes over a target (shaded region) buried in very wet clayey soil, frozen and unfrozen.

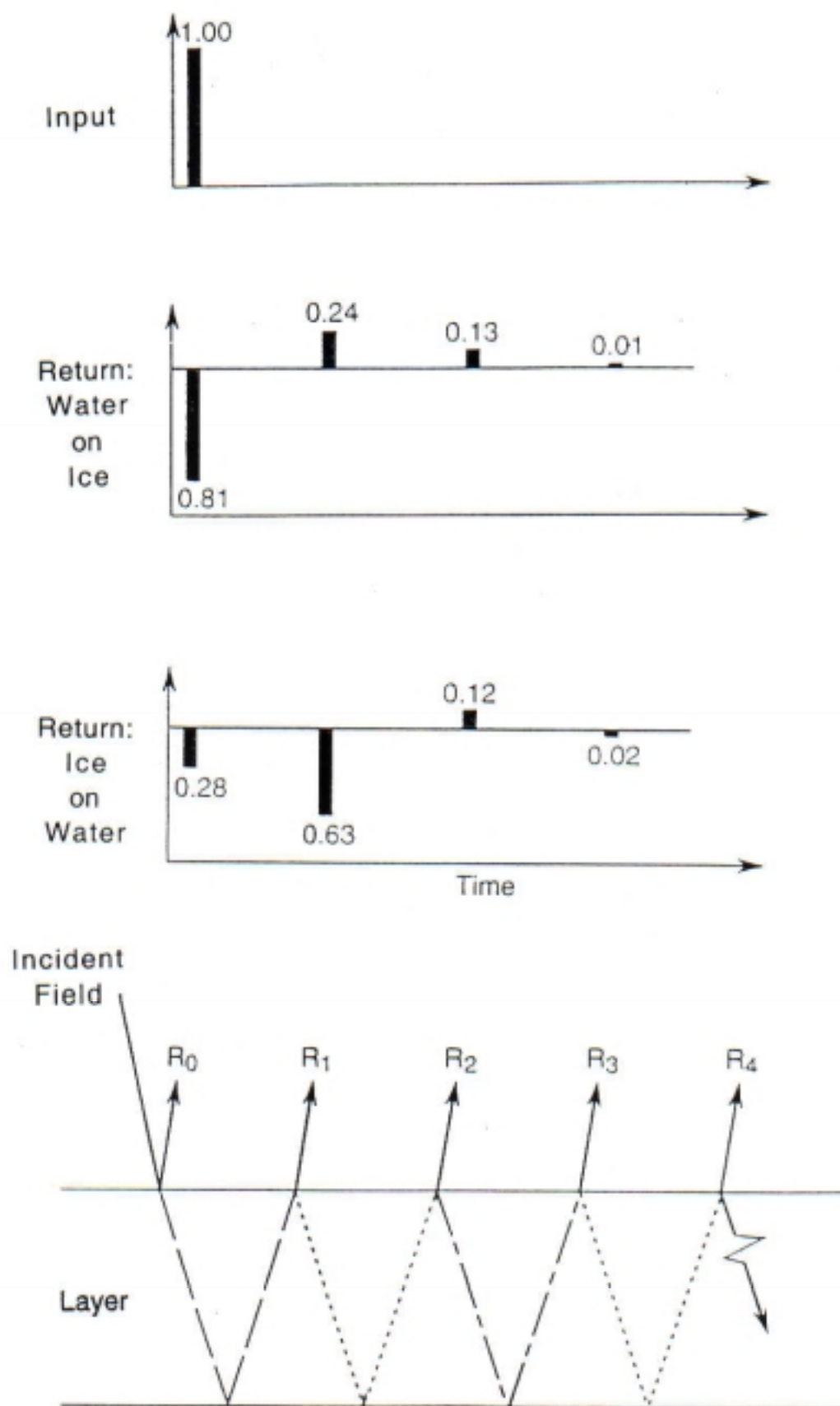


FIGURE 1.

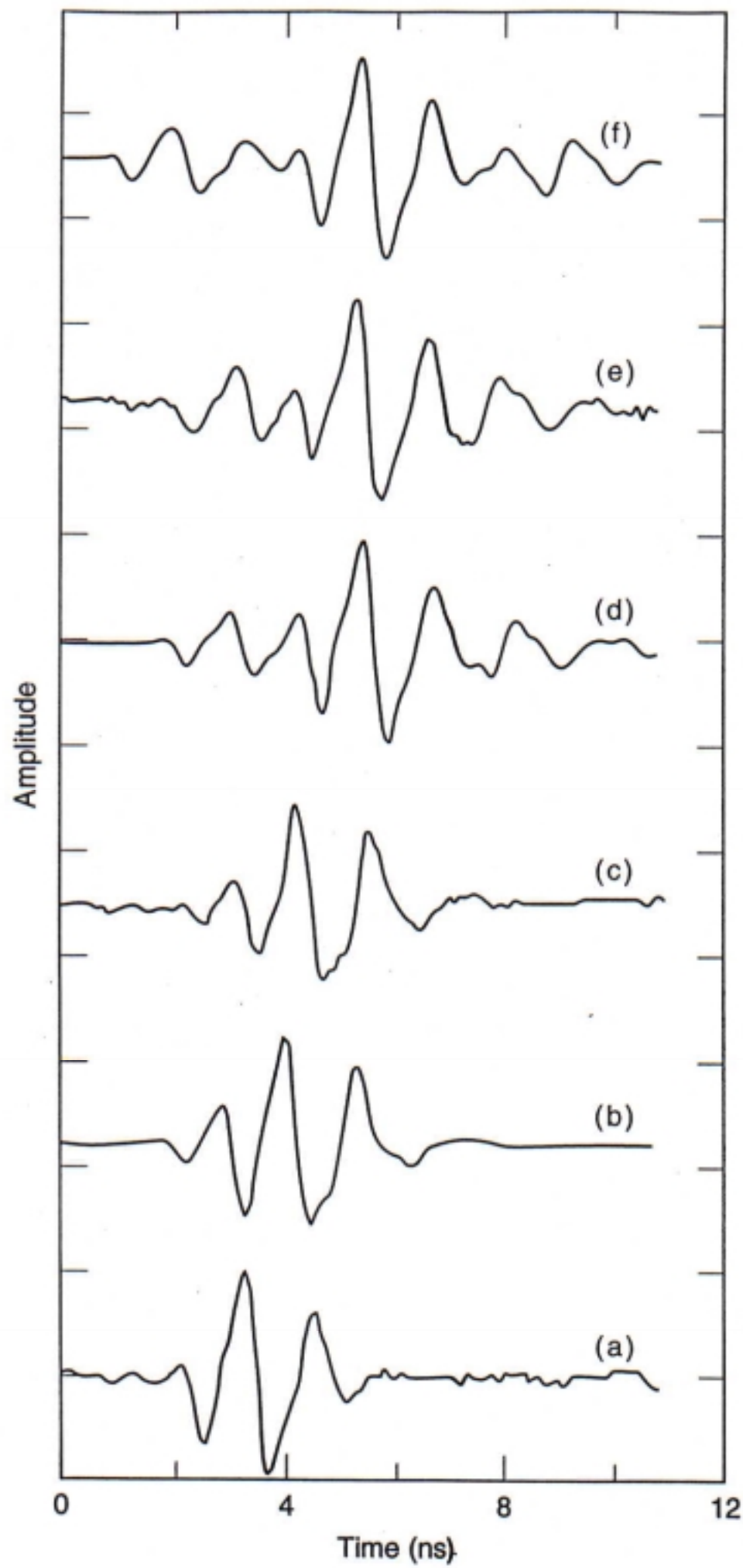


FIGURE 2.

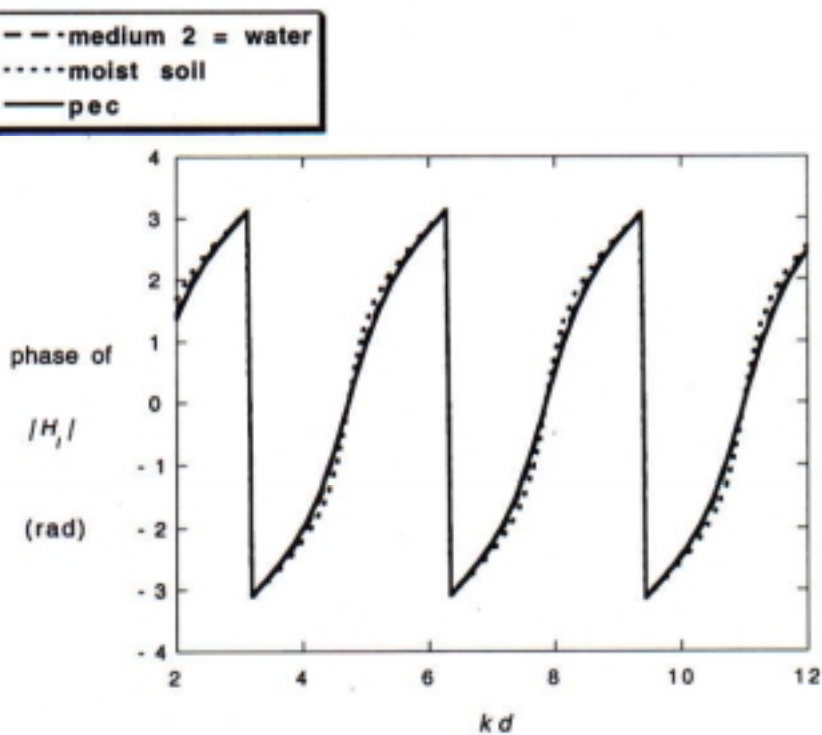
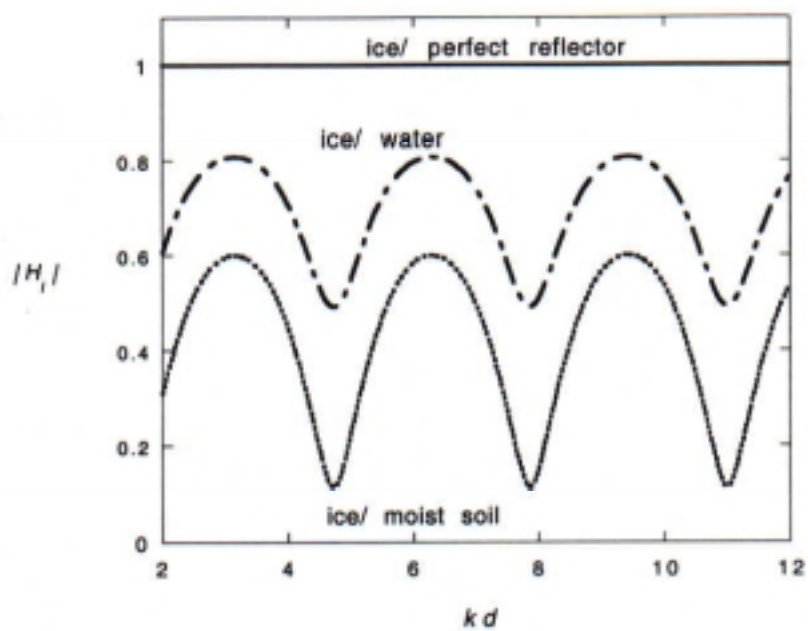


FIGURE 3.

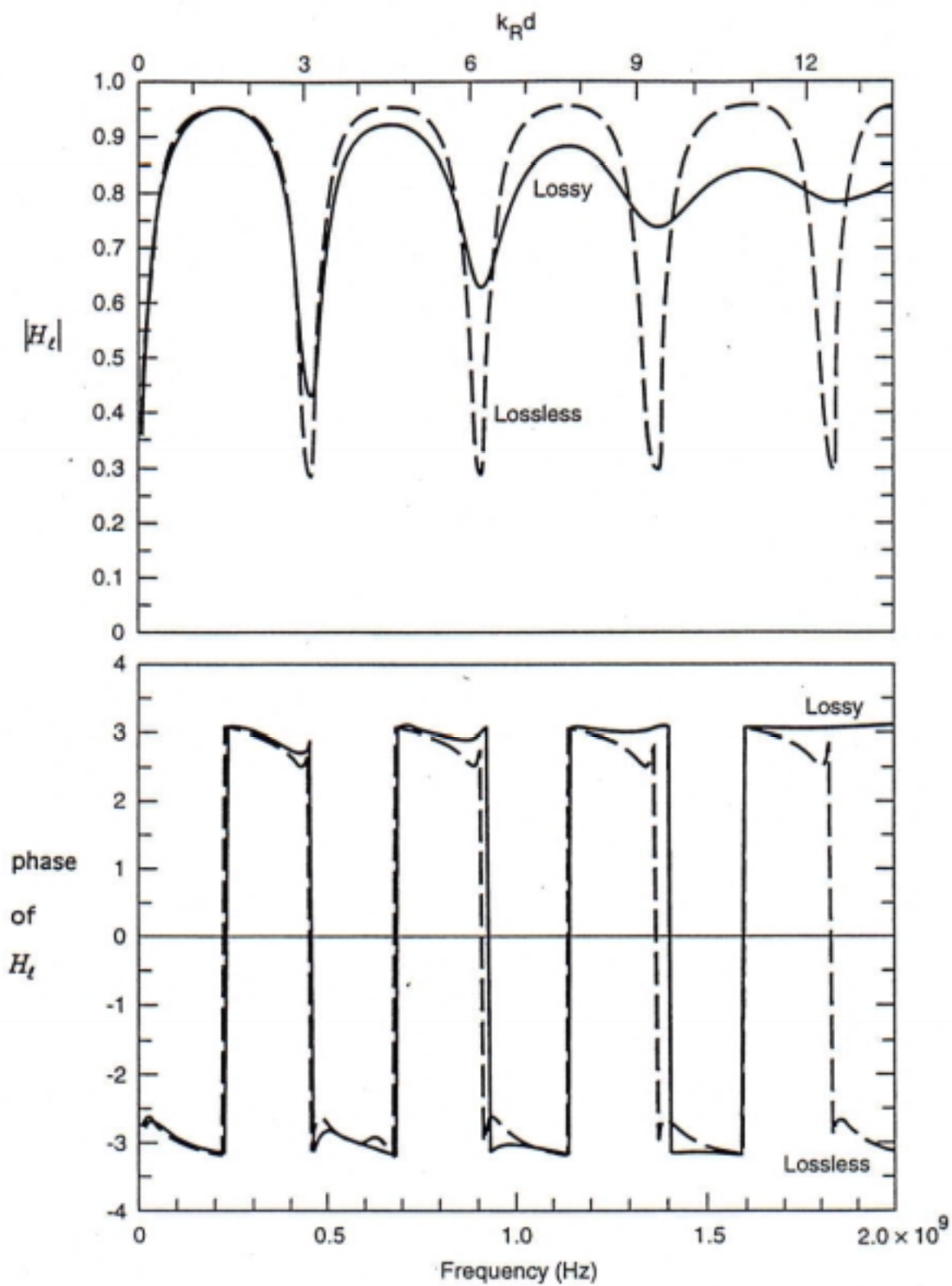


FIGURE 4.

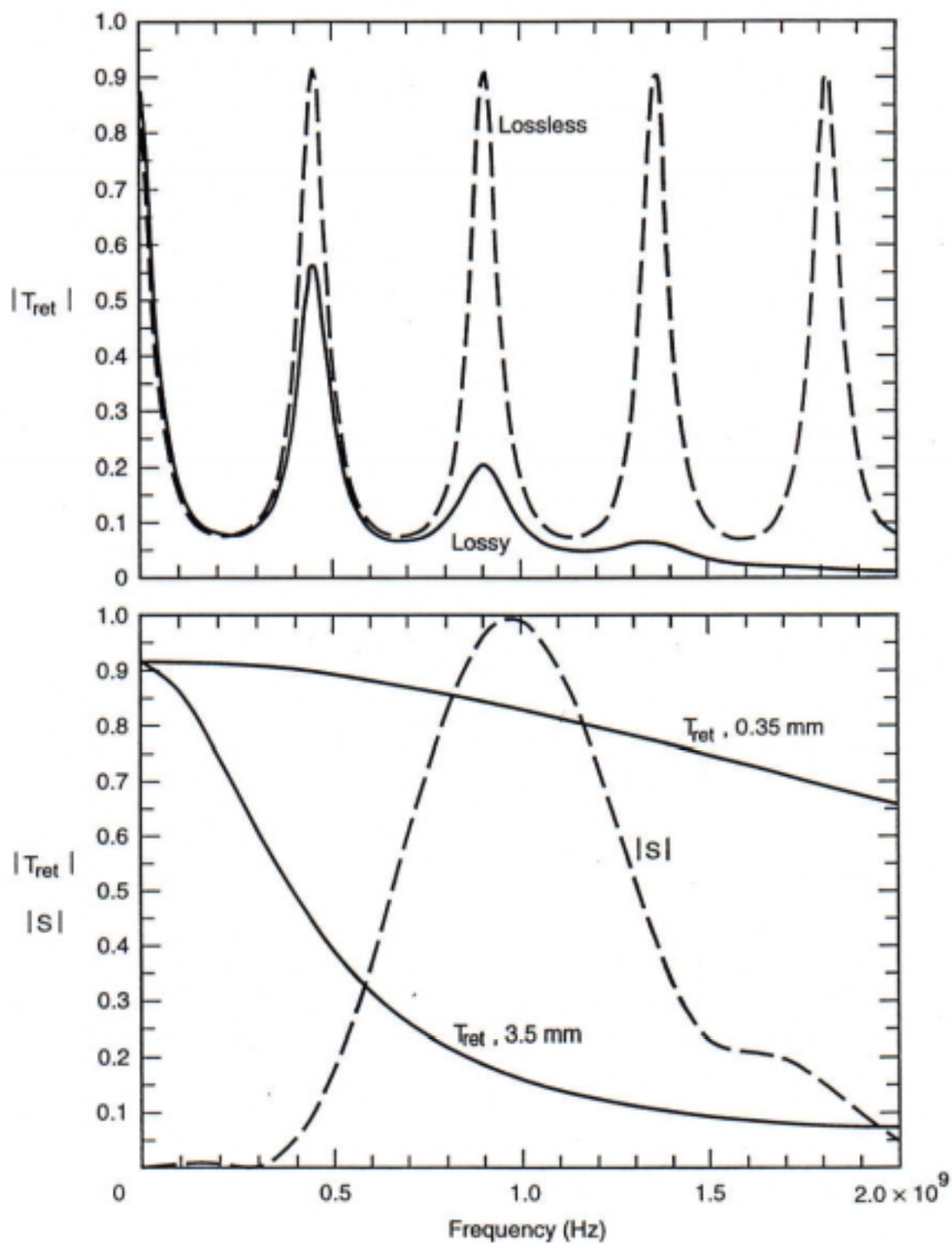


FIGURE 5.

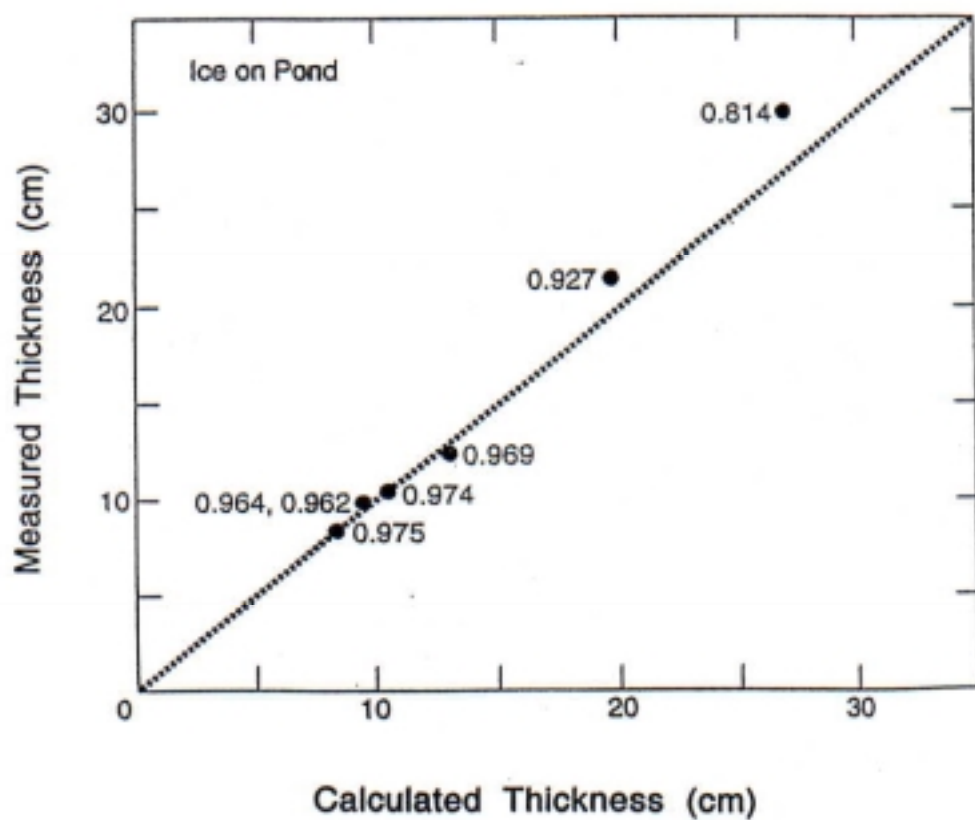
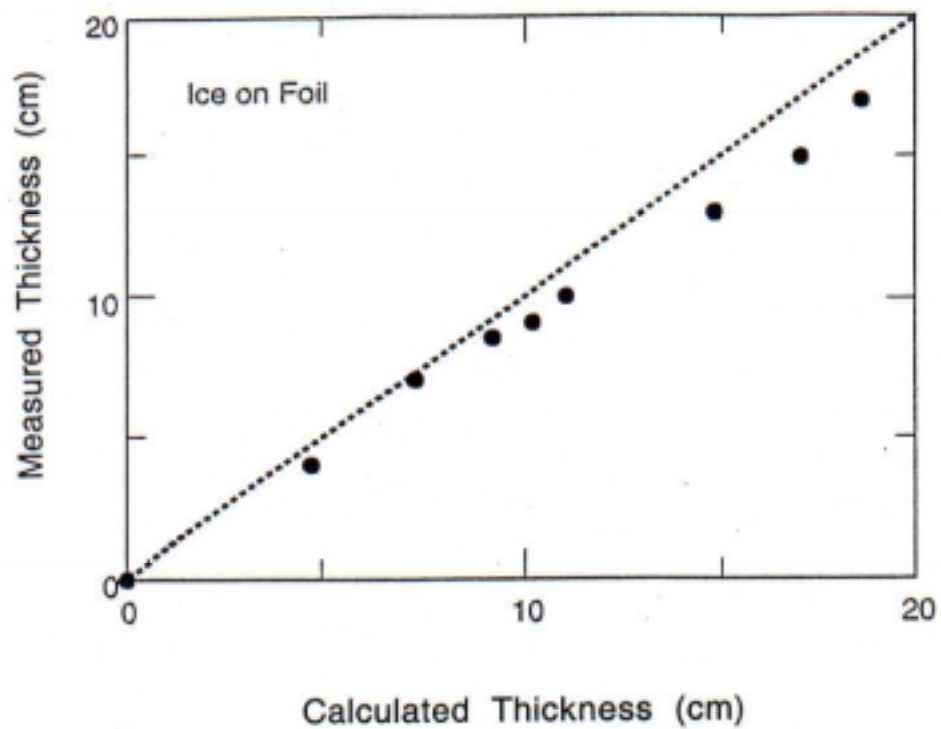


FIGURE 6.

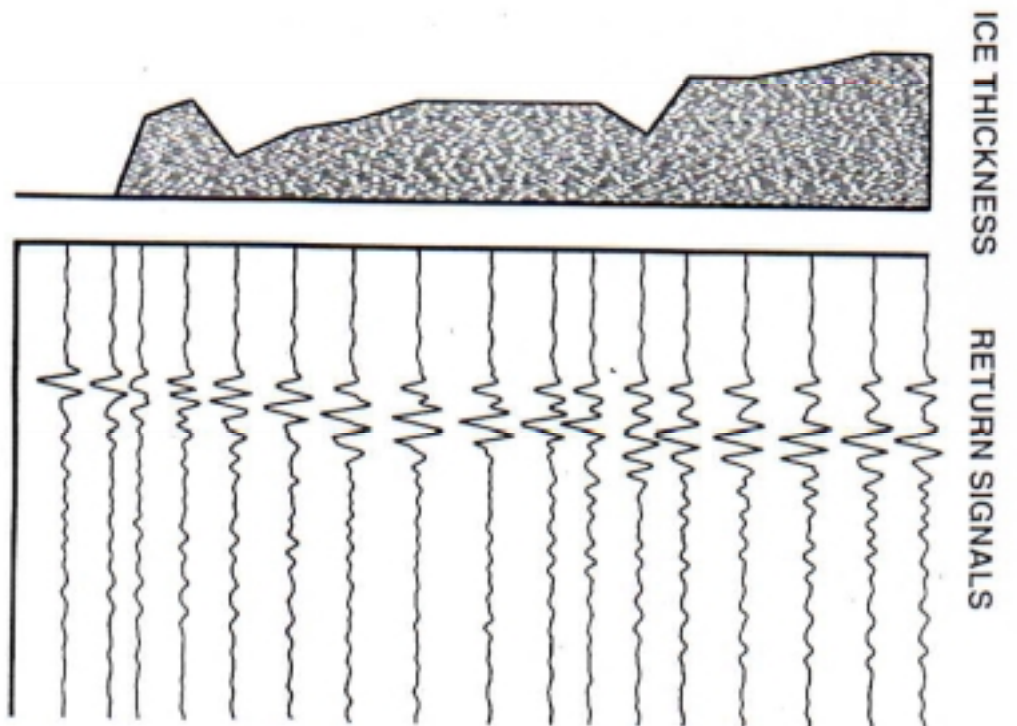


FIGURE 7.

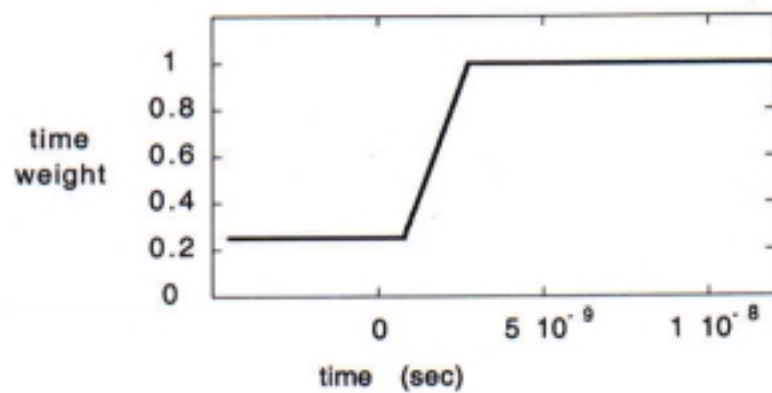
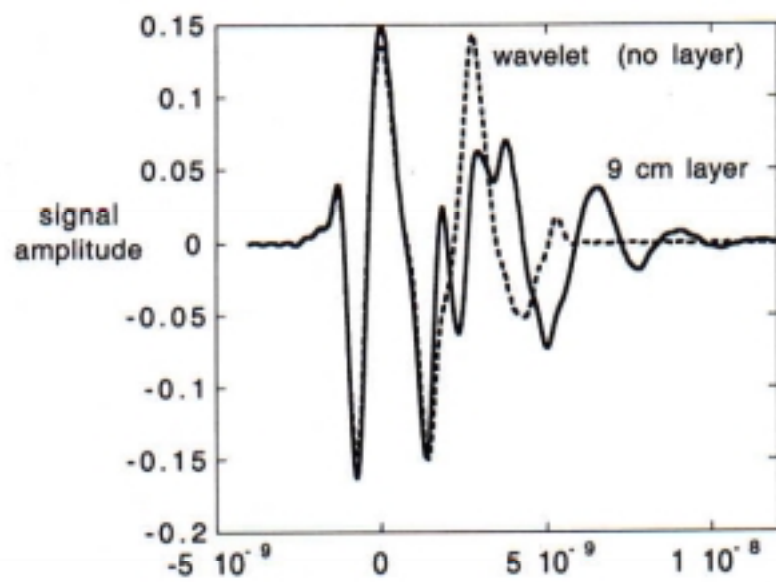
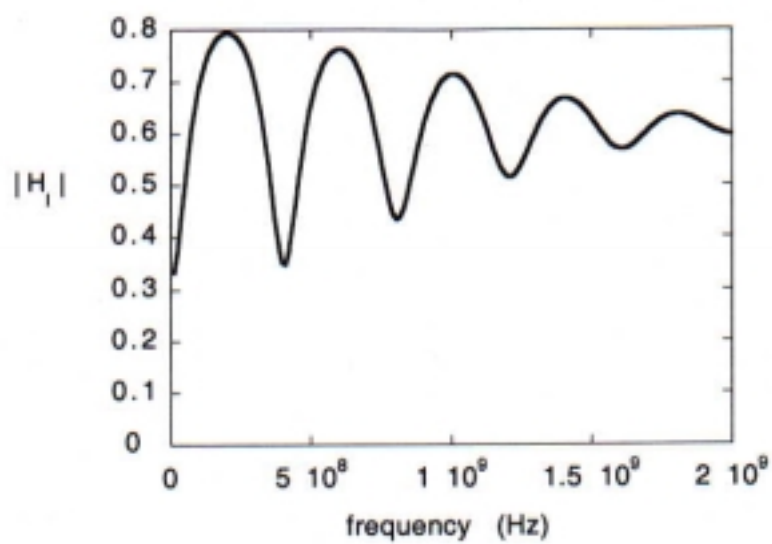


FIGURE 8.

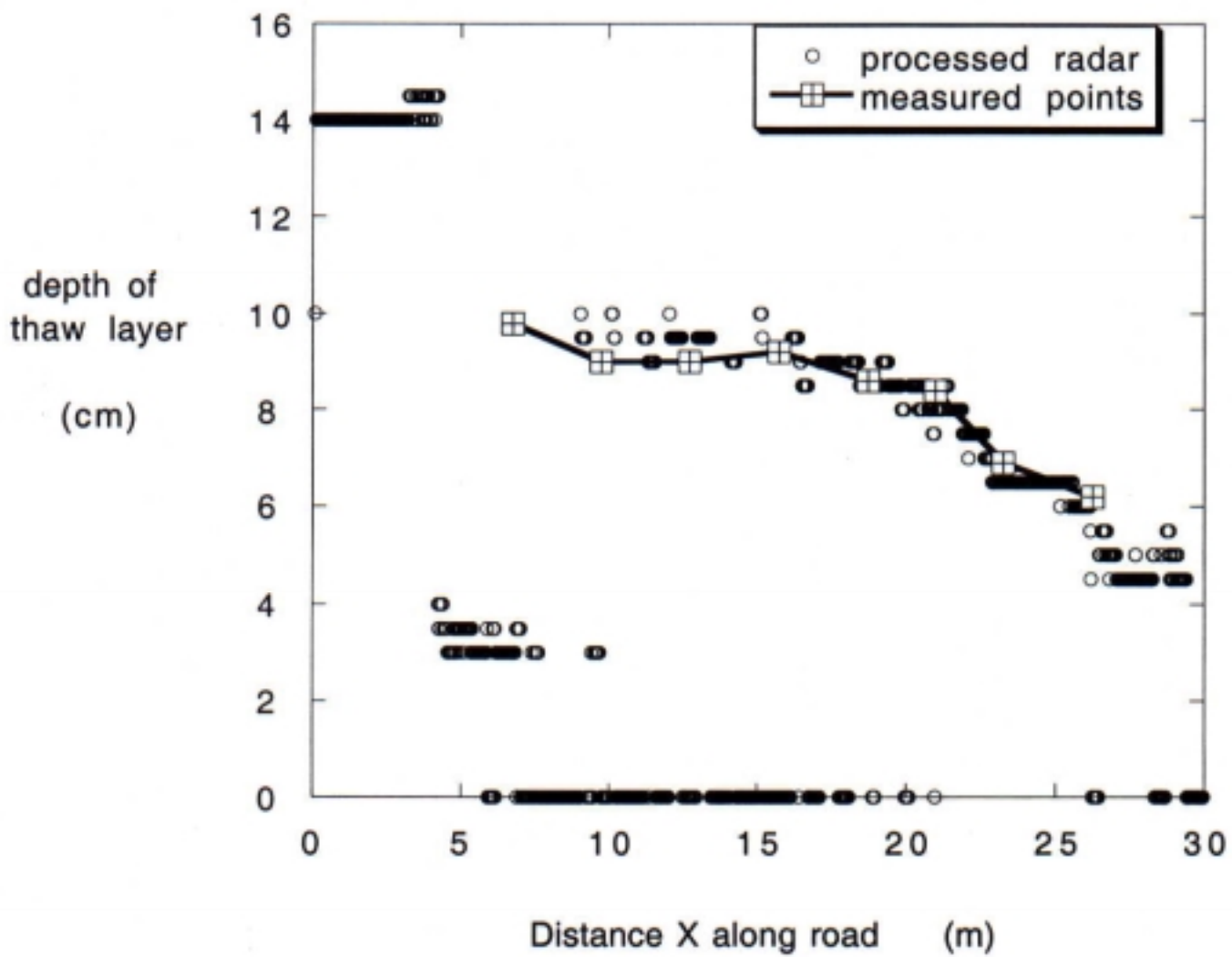


FIGURE 9.

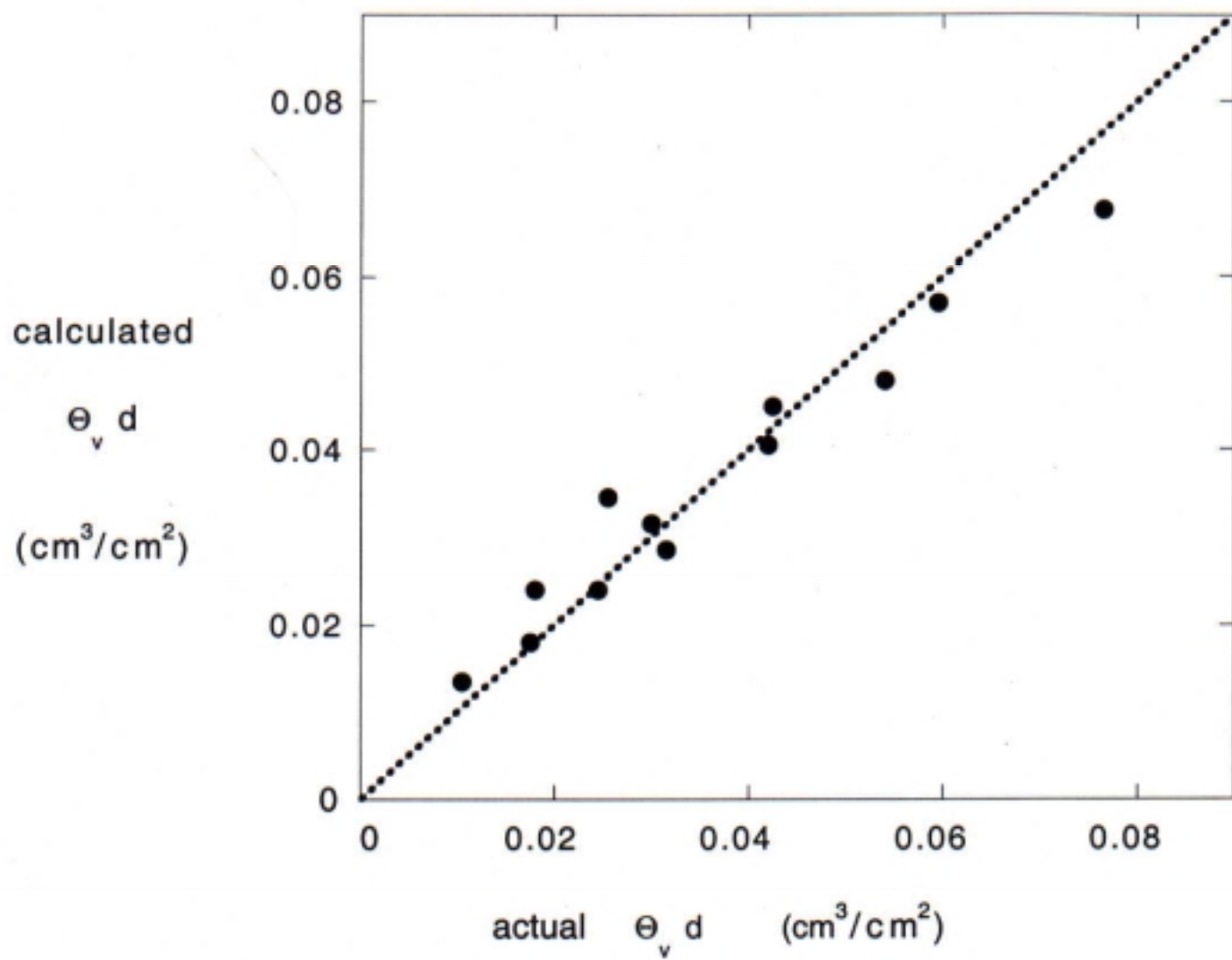


FIGURE 10.

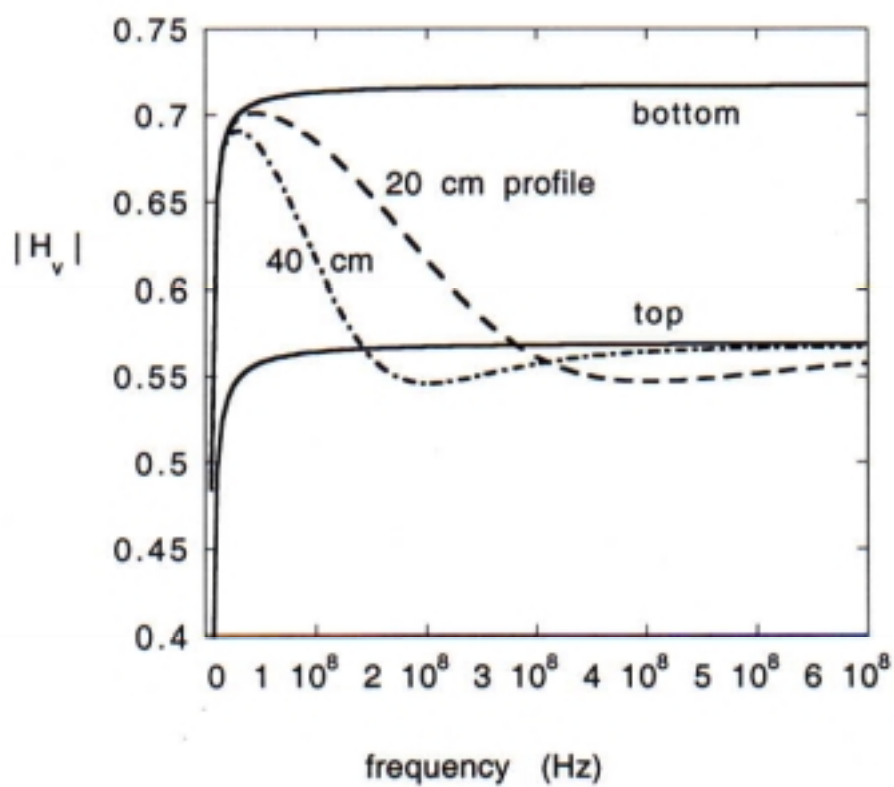
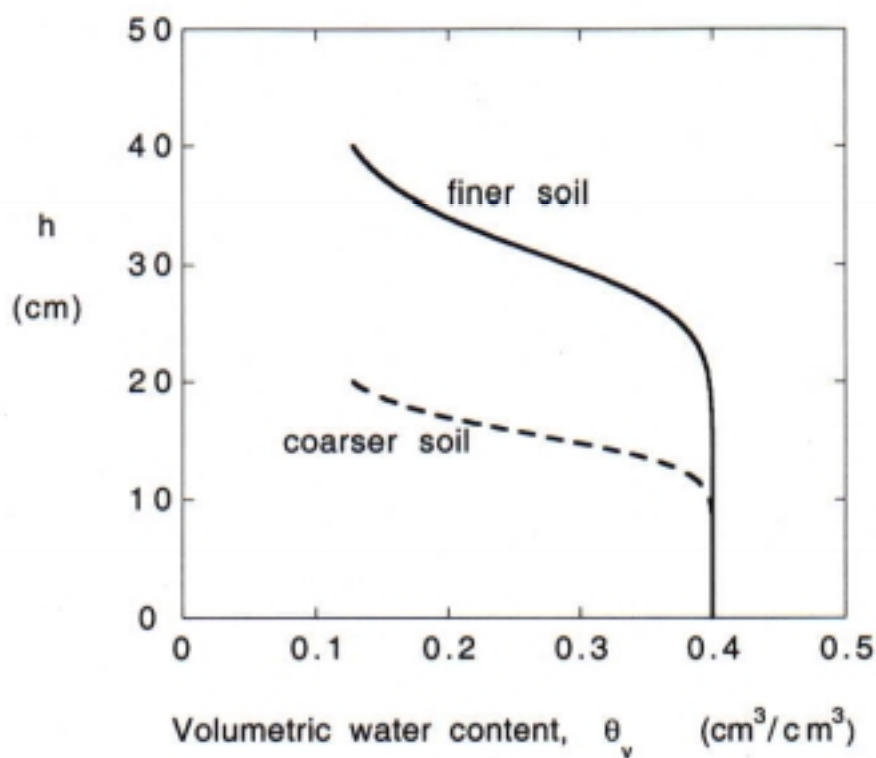


FIGURE 11.

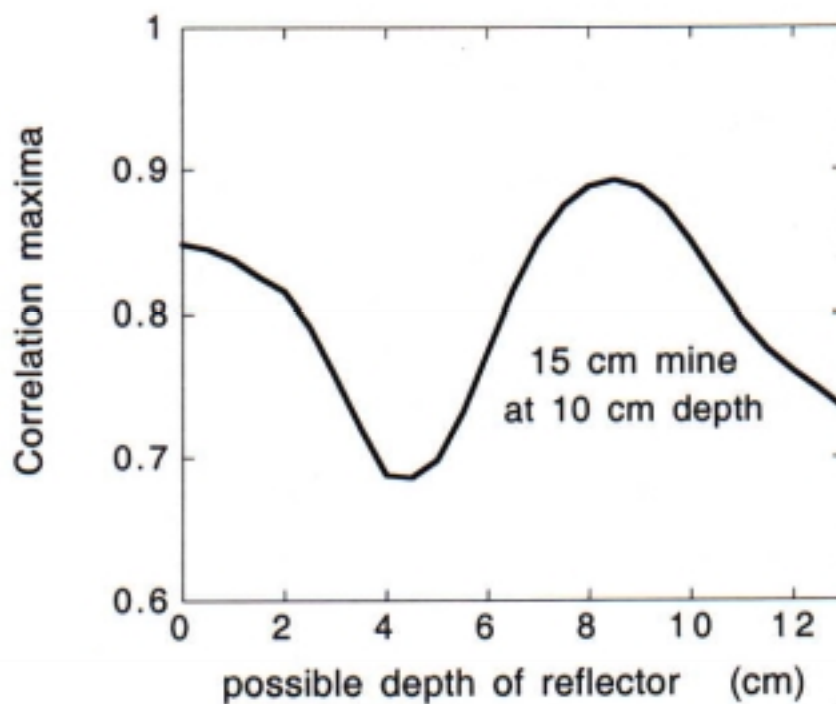
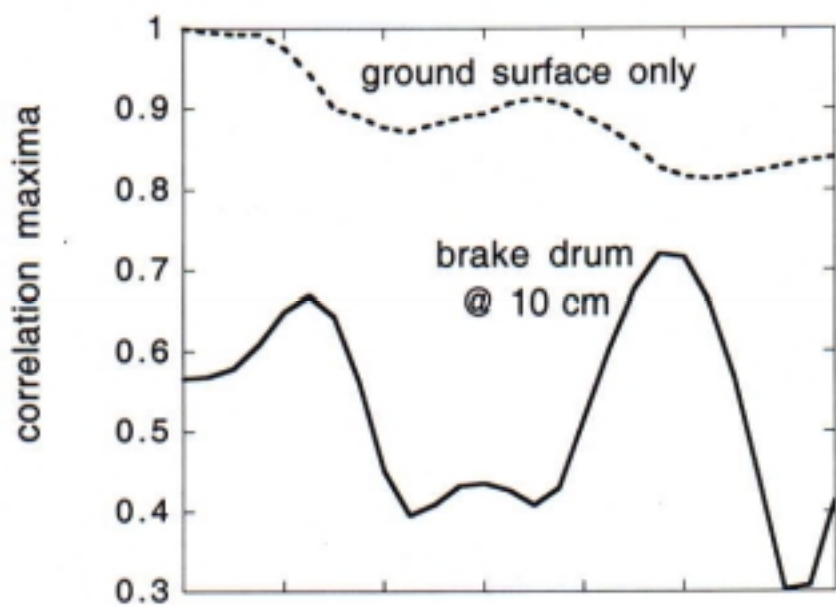


FIGURE 12.

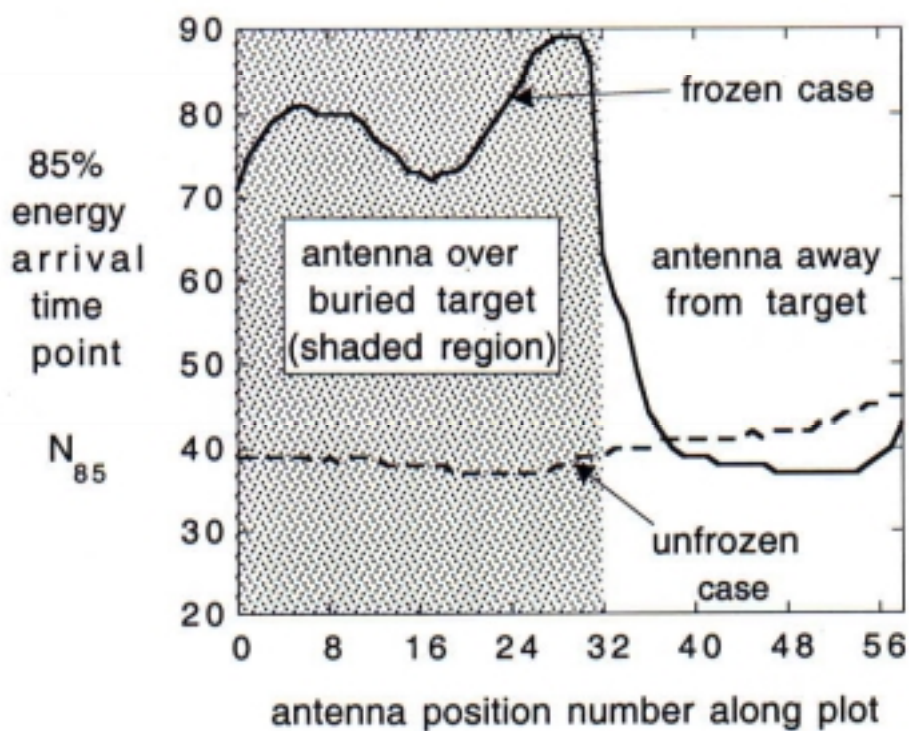
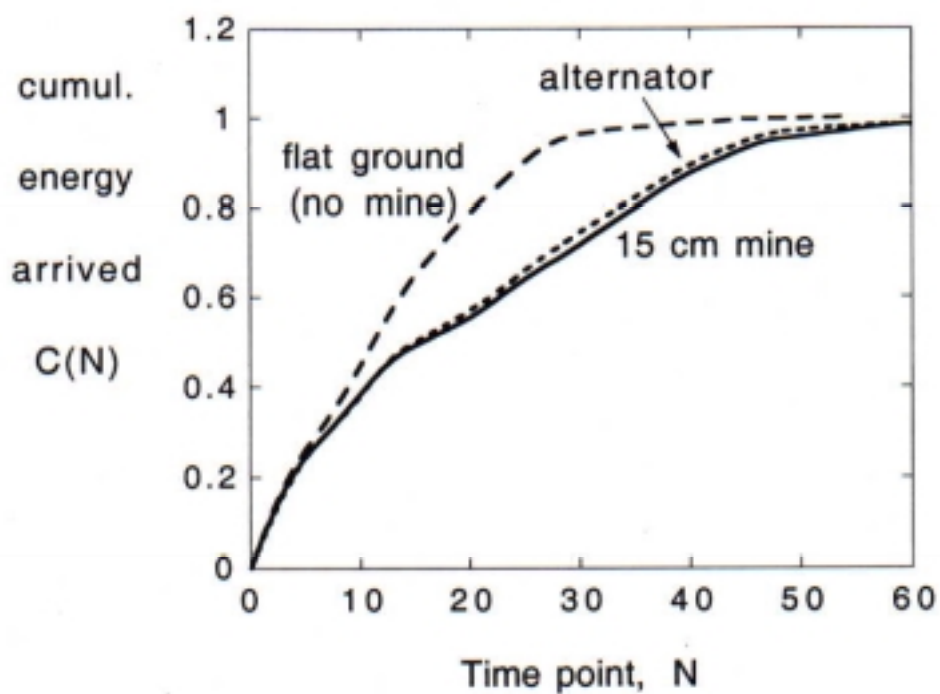


FIGURE 13.